Effect of charge and anisotropic diffusivity on ion exchange kinetics in nuclear waste form materials

Yulan Li, Shenyang Hu, Robert Montgomery, Agnes Grandjean, Theodore Besmann, Hans-Conrad Zur Loye

Effect of Charge and Anisotropic Diffusivity on Ion Exchange Kinetics in Nuclear Waste Form Materials

Yulan Li[a*], Shenyang Hu[a#], Robert Montgomery[a], Agnes Grandjean[b], Theodore Besmann[c], and Hans-Conrad zur Loye[c]

[a] *Pacific Northwest National Laboratory, Richland, WA 99352*

[b] *CEA, DEN, Univ Montpellier, Research Department on Enrichment, Dismantling and Waste Technologies, SEAD/LPSD, Marcoule, BP 71171, 30207 Bagnols-sur-Cèze cedex, France*

[c] *Department of Chemistry and Biochemistry, University of South Carolina, Columbia, SC 29208, USA*

[*]Corresponding author: yulan.li@pnnl.gov

[#]Corresponding author: shenyang.hu@pnnl.gov

Abstract

Motifs of radionuclide absorption particles (absorbers or fillers) for the nuclear waste treatment usually have crystal structures with nano-sized tunnels for fast ion diffusion. On the other hand, the accumulation of ions generates an electric field which affects the ion diffusion. Therefore, the strong anisotropic kinetic properties and the electric field affect ion exchange kinetics, especially in an assembly of these particles which may block the fast diffusion tunnels for each other. In this work, we developed a mesoscale model to describe the effect of anisotropic kinetic properties and electric field on ion exchange kinetics. With the model we simulated the effect of anisotropic diffusivity, electrochemical potential, particle morphology, size and aggregation on ion exchange kinetics during batch experiments. It is found that 1) ion exchange results in charge accumulation inside the particle because different ions have different diffusivities and different diffusion driving forces. The electric neutrality is not preserved; 2) the electric field speeds up the slower diffusion ions (either uptake or release) and slows down the faster diffusion ions to reduce charge accumulation and maintains charge neutrality; 3) the ion exchange becomes very slow at the later stages because a) diffusion driving force (electrochemical gradient, Cs^+ concentration in the solution and Na^+ inside the particle) continuously decreases, as observed in batch experiments; and b) the diffusivity decreases due to the Cs^+ concentration dependence of ion diffusivity. This can explain the observed experimental phenomena that the radionuclide

capacity usually cannot be reached; 4) for needle-like particle and their clusters, both surface area and diffusion distance along the direction with the fastest diffusivities have significant impact on the ion exchange kinetics.

Key words: Ion exchange kinetics; ion charge; anisotropic diffusivity; nuclear waste form.

1. Introduction

Radioactive effluents containing cesium and strontium isotopes are generated from nuclear power plants, radioactive nuclear fuel processing plants, and other nuclear facilities. These radioisotopes with half-lives of around 30 years [1] are soluble in water and extremely hazardous in the environment [2]. Therefore, they must be removed from wastewater resulting from ongoing nuclear energy generation as well as radiation clean-up activities. Hierarchical materials that have nano-sized tunnel networks and/or multiple porous structures have attracted much interest as candidate waste forms due to the potential to tailor their molecular/crystal lattice and higher scale features to immobilize specific radionuclides in an optimized matrix [3]. These hierarchical materials contain nanostructured fillers that are being developed to absorb and remove radionuclides from waste streams, for example, zeolites [4-7], hexacyanoferrates (metal-HCFs) [8-12], hollandites [13-17], zirconium-containing metal-organic frameworks (MOFs)[18] and uranium salt inclusion materials (SIMs) [19]. In these materials, the common feature of their crystal structures is nano-sized cage networks and/or pore tunnels which allow the fast diffusion of radionuclides during ion exchange (or leaching) and have a high capacity for radionuclides. The crystalline tunnel structures imply anisotropic thermodynamic and kinetic properties which were demonstrated from experiments[20] and atomistic simulations[12, 21, 22]. The faceted and needle-like morphologies of their single crystals as shown in Fig. 1 also indicate anisotropic thermodynamic and kinetics properties[3]. For engineering applications, it is often necessary to sinter these crystalline particles to bulk waste form materials with macro, meso- and nano-pores providing large free surface to enhance the ion exchange efficiency[5, 20, 23]. However, the aggregation of nano-sized particles may block the fast diffusion tunnels. As a result, ions might accumulate and generate an electric field, especially in saline wastewater; both fast diffusion tunnel blocking, and electric field may affect ion exchange kinetics.

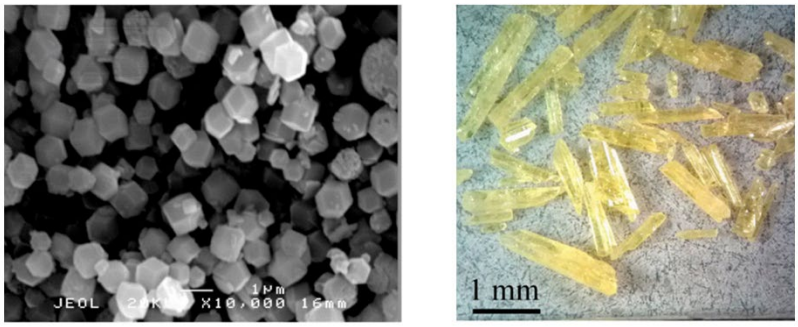

(a) (b)

Fig. 1. (a) SEM image of LTA-zeolite particles (NaAlSiO4)[24]; (b) Optical image of salt inclusion single crystals [25-27].

In our previous work[28], a mesoscale model was developed to simulate the effect of particle aggregation on ion exchange kinetics. In this work, we extended the model to consider the effect of anisotropic kinetic properties and ion electric interactions on ion exchange. Batch experiments are commonly used to measure the adsorption equilibrium and kinetics of adsorbent materials in a liquid solution, which can provide the thermodynamic and kinetic properties required in the model and validate the model. The ion exchange between Na^+ and Cs^+ in Na-zeolite particles in batch experiments was taken as a model system to describe the model [24, 29]. In fact, radionuclides leaching from zeolite particles is the reverse process of uptake. Whether uptake or leaching occurs depends on the electrochemical potentials of ions inside the particle and the waste solution. Therefore, the model enables one to study the effect of particle morphologies, particle aggregation and microstructure in composites on ion exchange or leaching kinetics in the environment and materials of interest.

2. Description of ion exchange model

We considered a batch experiment in which a certain volume or weight fraction of radionuclide absorption particles were added into a container with nuclear waste solution resulting in ion exchange which is driven by the electrochemical potential difference of ions inside the particles and in the solution. A simulation cell consisting of liquid solution and solid particles is shown in Fig. 2. The coordinate system used in the analysis is as follows: $\mathbf{r} = (x_1, x_2, x_3)$ represents the global coordinate while (y_1, y_2, y_3) defines the orientation of single crystal particles in the global coordinate. We used $c_i(\mathbf{r}, t)(i = 1, \mathrm{Na}^+; i = 2, \mathrm{Cs}^+)$ to describe the

spatial distributions of Na^+ and Cs^+ concentrations, respectively. The order parameter field $\eta_\alpha(\mathbf{r})$ was employed to describe different phases/particles. In particular, η_1 refers to the liquid phase and η_α (α =2, ⋯, N) refer to the solid particles. Different order parameters were used for different particles to distinguish that they may have different orientations and morphologies from each other. We utilized $\varphi(\mathbf{r}, t)$ to describe the electrostatic potential field due to the ion distribution.

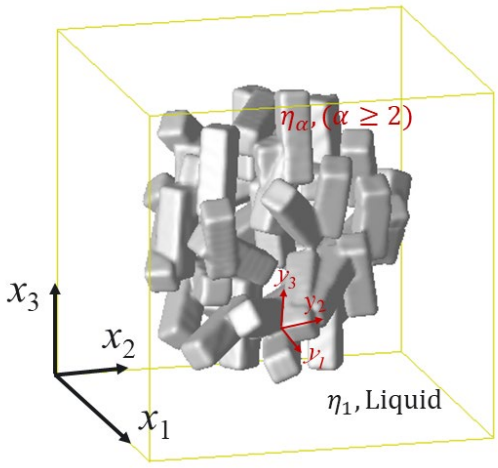

Fig. 2. Schematic of particle cluster and simulation cell. $\eta_\alpha = \eta_\alpha(\mathbf{r})$ is an order parameter to distinguish different phases/particles: α=1, liquid phase; $\alpha = 2, \cdots, N$, solid particles. N=2 refers to the case with a single particle or a cluster with particles well separated.

The uptake of Cs^+, i.e., diffusion and exchange of Na^+ and Cs^+, in the hierarchical structure (the cluster of particles) are described by the Cahn-Hilliard equations:

$$\frac{\partial c_i(\mathbf{r},t)}{\partial t} = \nabla \cdot \left(\mathbf{D}_i \nabla \left(\frac{\mu_i}{RT} \right) \right), \quad i = 1, \mathrm{Na}^+; i = 2, \mathrm{Cs}^+, \tag{1}$$

where c_i, $\mathbf{D}_i$ and μ_i are, respectively, the concentration, diffusivity tensor, and chemical potential of species i. R and T are the ideal gas constant and the absolute temperature, respectively. $R = 8.314\ [\frac{\mathrm{J}}{\mathrm{mol\ K}}]$, and T is in K. The diffusivity tensor, $\mathbf{D}_i = \{D_{i,kl}\}$, is a symmetric positive definite matrix, in general, by considering anisotropic diffusion and $D_{i,kl}$ $(k, l = 1,2,3)$ is a component of $\mathbf{D}_i$. t is time and $\nabla = \left(\frac{\partial}{\partial x_1}, \frac{\partial}{\partial x_2}, \frac{\partial}{\partial x_3} \right)$. Any letter with boldface represents a tensor matrix or a vector in this work. Under the given boundary conditions and initial conditions, we can obtain the spatial and temporal evolution of concentration c_i by solving eq. (1).

In the model system, there are two phases: radionuclide absorption particles (such as zeolite or salt inclusion compound) and liquid solution. The chemical free energy of species *i* (Na^+ or Cs^+) near equilibrium can be approximated by a parabolic function of Na^+ and Cs^+ concentrations [30]. Since the chemical potential is the derivative of the chemical free energy with respect to concentration, the chemical potential of species *i* in the multiple phase/particle (*N*) system can be described as:

$$\mu_i = RT \sum_{\alpha=1}^{N} A_i(\alpha) \left(c_i - c_i^{eq}(\alpha)\right) \eta_\alpha, \quad i = 1, 2, \tag{2}$$

where $c_i^{eq}(\alpha)$ (*i*=1, 2) is the equilibrium concentrations of Na^+ and Cs^+ in phase α, respectively. In addition to the dimensionless concentrations c_i (including c_i^{eq}), $A_i(\alpha)$ is a dimensionless free energy coefficient of phase/particle α (α = 1, 2, ⋯, N) that corresponds, respectively, to liquid phase (α =1) and radionuclide absorption particles (α =2, ⋯, N). The equilibrium concentrations $c_i^{eq}(\alpha)$ and coefficients $A_i(\alpha)$ can be determined once we know the free energies of these phases/particles. The order parameter $\eta_\alpha = \eta_\alpha(\mathbf{r})$ was used to distinguish different phases/particles and has its definition as $\eta_\alpha(\mathbf{r}) = 1$ when $\mathbf{r}$ is inside phase/particle α and $\eta_\alpha(\mathbf{r}) = 0$ once $\mathbf{r}$ is outside phase/particle α. $\eta_\alpha(\mathbf{r})$ varies continuously from 1 to 0 across the interface of phase/particle α and its neighboring phases. In this work, the order parameters are spatially dependent but don't evolve with time. They were obtained by running a phase field model of particle nucleation and growth which is similar to the grain growth model[31]. Controlling the nucleation densities, nucleus sizes, and growth rates, a 3D hierarchical structure as shown in Fig. 2 or a single particle with different morphologies can be obtained. These order parameters vary smoothly from 1 to 0 across particle surfaces. The spatial distributions of the corresponding order parameters are used to describe the inhomogeneous and anisotropic kinetic properties in the ion exchange model.

Diffusivity tensor $\mathbf{D}_i$ can be different in different phases/particles. $\mathbf{D}_i$ is usually much larger on interfaces and grain boundaries than inside the particles. Since Na^+ and Cs^+ diffuse through porosity in the form of channels and only occupy certain lattice sites in zeolites, the occupation of Na^+ and Cs^+ inside zeolite crystals changes the chemistry, which may result in lattice distortions and/or phase transitions. As a result, the diffusivity may strongly depend on the concentrations of Na^+ and Cs^+. Therefore, the diffusivity of Na^+ and Cs^+ are spatial and

concentration dependent. The following equation was used to describe the inhomogeneous diffusivity in this work:

$$D_{i,kl}(\mathbf{r}) = \xi_i(c_2, \Phi) \sum_{\alpha=1}^{N} h(\alpha) D_{i,kl}^{(\alpha)}, \tag{3}$$

where $D_{i,kl}^{(\alpha)}$ is the diffusivity component of species i in phase/particle α and a constant.

$$h(\alpha) = \begin{cases} 1.0, \eta_\alpha \geq \eta_{crit} = 0.5, \\ 0.0, \eta_\alpha < \eta_{crit} = 0.5, \end{cases} \tag{4}$$

$$\xi_i(c_2, \Phi) = 1 + \frac{d_{i,inh}}{\exp\left(-k\left[\left(\frac{c_2}{c_2^{eq,S}}\Phi\right)^2 - a_k\right]\right)+1}, \; c_2 = c_{Cs^+}, \Phi = \sum_{\alpha=2}^{N} \eta_\alpha^2. \tag{5}$$

Function $h(\alpha)$ in eq. (4) is a sharp description cross the interface of neighboring particles or the interface of solid phase and liquid phase. It is used to distinguish different particles or phases having different diffusion anisotropy. As $\eta_\alpha = 1, (\alpha = 2, \cdots, N)$ represents the radionuclide absorption solid particle α, $\Phi = 1$ refers to the solid phase consisting of all solid particles considered; $\Phi = 0$ refers to the liquid phase. $0 < \Phi < 1$ refers to the interface between the solid phase and liquid phase or between the solid particles. The variables $d_{i,inh}$, k, and a_k are model parameters to describe the concentration c_2 and structure Φ dependence of diffusivity. $c_2^{eq,S} = c_2^{eq}(S)$ is the equilibrium concentration of c_2 in the solid particle phase.

During ion exchange, a phase transition takes place from initial Na^+ rich zeolite phase with concentration ($c_1^0(S) = 1.0$, $c_2^0(S) = 0.0$ or a small value such as 0.00001 used in the simulations) to Cs^+ rich zeolite phase with an equilibrium concentration with ($c_1^{eq}(S) = 0.001, c_2^{eq}(S) = c_2^{eq,S} = 1.0$). Because the atomic volumes of Na^+ and Cs^+ are different, the lattice distortion and chemistry change with the exchange of Cs^+ for Na^+, which affects the diffusion barrier of Na^+ and Cs^+ in the zeolite. We designed the concentration dependent function described by eq. (5) to capture the diffusivity change due to the transition from the Na^+ rich phase to the Cs^+ rich phase.

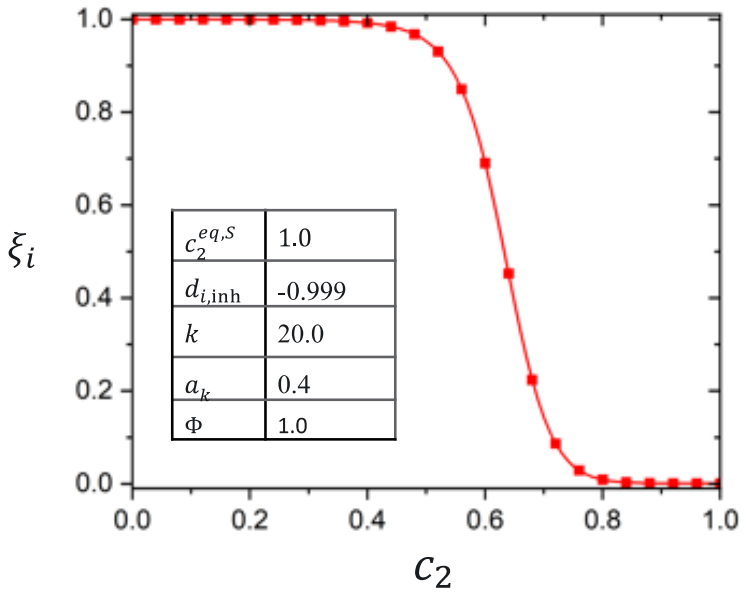

Fig. 3. Function $\xi_i(c_2, \Phi = 1)$ in eq. (5) with the parameters listed in the inset varying from 1 to 0.001 with the increases of concentration c_2 from 0 to 1.

For given model parameters k, a_k, $d_{i,inh}$, $c_2^{eq,S}$, and $\Phi = 1$, Fig. 3 shows the variation of $\xi_i(c_2, \Phi = 1)$ in terms of c_2. From Fig. 3 we can see that when concentration c_2 changes from 0 to $c_2^{eq,S} = 1$, $\xi_i(c_2, \Phi = 1)$ varies from 1 to $(1 + d_{i,\mathrm{inh}})$. Thus, the diffusivities $D_{i,kl}$ of Na^+ (i=1) and Cs^+ (i=2) change accordingly. For example, inside of particle η_2 (where $\eta_2 = 1$, therefore, $\Phi = 1$) the diffusivity changes from $D_{i,kl}^{(2)}$ (Na^+ rich zeolite phase) to $(1 + d_{i,\mathrm{inh}})D_{i,kl}^{(2)}$ (Cs^+ rich zeolite phase) when c_2 changes from 0 to $c_2^{eq,S}$. When c_2 is between these two phases, the associated diffusivity varies smoothly from $D_{i,kl}^{(2)}$ to $(1 + d_{i,\mathrm{inh}})D_{i,kl}^{(2)}$. It requires a concentration dependent diffusion barrier to accurately describe the change for the intermediate concentration c_2. In principle, the concentration dependence of the diffusion barrier could be obtained from the density function theory (DFT) calculations. But these data are not available now for the system of interest. Therefore, we used the concentration dependence described in eq. (5). In phase-field models, a shape function like $\xi_i(c_2, \Phi)$ is often used to construct microstructure and concentration dependence of thermodynamic and kinetic properties [28]. A specific functional may affect the driving force or kinetics but it should qualitatively capture the physics. Similarly, the functional $\xi_i(c_2, \Phi)$ also describes the diffusivity which smoothly changes from $D_{i,kl}^{(1)}$ (liquid

phase) to $D_{i,kl}^{(\alpha)}$ ($\alpha \geq 2$, solid phase) with the change of η_1 from 1 to 0 as well as a smooth change across the interface between any two solid particles.

To consider the effect of ion charge, the electrostatic potential φ from the charge density

$$\rho(\mathbf{r}) = \Omega \sum_{i=1}^{2} z_i [c_i(\mathbf{r}) - c_i^0(\mathbf{r})] \tag{6}$$

is integrated into the chemical potential:

$$\mu_i = RT \sum_{\alpha=1}^{N} A_i(\alpha) \left(c_i - c_i^{eq}(\alpha)\right) \eta_\alpha + F_c z_i \varphi, \;\; i = 1,2, \tag{7}$$

where $c_i^0(\mathbf{r})$ is the initial spatial distribution of $c_i(\mathbf{r})$. z_i is the valence of species i, and F_c is Faraday's constant, $F_c = 96485.33\ [\frac{\mathrm{C}}{\mathrm{mol}}]$. Ω is a conversion coefficient from dimensionless concentration to the unit of coulomb/m^3 or C/m^3. We assumed that there is no charge at initial stage and Na^+ and Cs^+ occupy the same lattice during ion exchange.

The electrostatic potential, φ, can be obtained by solving the Poisson's equation,

$$\nabla \cdot [\boldsymbol{\epsilon}(\mathbf{r}) \nabla \varphi] + \rho = 0 \tag{8}$$

where $\boldsymbol{\epsilon}(\mathbf{r}) = \{\varepsilon_{kl}(\mathbf{r})\}\epsilon_0$ is the dielectric permittivity tensor and $\epsilon_0 = 8.854 \times 10^{-12}\ \frac{\mathrm{F}}{\mathrm{m}}$ is the vacuum permittivity.

$$\varepsilon_{kl}(\mathbf{r}) = \sum_{\alpha=1}^{N} h(\alpha) \varepsilon_{kl}^{(\alpha)}, \tag{9}$$

where $\varepsilon_{kl}^{(\alpha)}$is the relative dielectric permittivity component in phase/particle α and a constant.

Since the considered particles may be anisotropic in diffusion and dielectric permittivity, coordinate transformation is needed to solve eqs. (1) and (8). Assume particle α has a coordinate transformation matrix $\{tr_{mn}(\alpha)\}$,

$$\{tr_{mn}\} = \begin{bmatrix} cos\,\psi_1\, cos\,\psi_2 - cos\,\theta\, sin\,\psi_1\, sin\,\psi_2 & -cos\,\psi_1\, sin\,\psi_2 - cos\,\theta\, sin\,\psi_1\, cos\,\psi_2 & sin\,\theta\, sin\,\psi_1 \\ sin\,\psi_1\, cos\,\psi_2 + cos\,\theta\, cos\psi_1\, sin\,\psi_2 & -sin\,\psi_1\, sin\,\psi_2 + cos\,\theta\, cos\,\psi_1\, cos\,\psi_2 & -sin\,\theta\, cos\psi_1 \\ sin\,\theta\, sin\,\psi_2 & sin\,\theta\, cos\,\psi_2 & cos\,\theta \end{bmatrix}, \tag{10}$$

where $\{\psi_1, \theta, \psi_2\}$ are the three Euler angles of the crystal axes (y_1, y_2, y_3) of the solid particle α rotating from the reference coordinates (x_1, x_2, x_3). In the reference coordinates (x_1, x_2, x_3),

$$D_{i,kl}^{(\alpha)} = \sum_{m=1}^{3} tr_{km}(\alpha) \sum_{n=1}^{3} tr_{ln}(\alpha) D_{i,mn}^{(0,\alpha)}, \tag{11}$$

$$\varepsilon_{kl}^{(\alpha)} = \sum_{m=1}^{3} tr_{km}(\alpha) \sum_{n=1}^{3} tr_{ln}(\alpha) \varepsilon_{mn}^{(0,\alpha)}, \tag{12}$$

where $\varepsilon_{mn}^{(0,\alpha)}$ and $D_{i,mn}^{(0,\alpha)}$ are, respectively, the components of the relative dielectric permittivity and diffusivity of phase α in its local coordinate. $\varepsilon_{mn}^{(0,\alpha)}$=$\varepsilon_{mn}^{S}$ when $\alpha \geq 2$; $\varepsilon_{mn}^{(0,1)}$=ε_{mn}^{L}. $\varepsilon_{mn}^{\mathrm{S}}$ and ε_{mn}^{L} are the relative dielectric constants in the solid crystal under its lattice coordinate and in the liquid, respectively. Same are for $D_{i,mn}^{(0,\alpha)}$, $D_{i,mn}^{(0,\alpha)}$=$D_{i,mn}^{S}$ when $(\alpha \geq 2)$ and $D_{i,mn}^{(0,1)}$=$D_{i,mn}^{L}$.

For cubic and needle particles, the diffusivity may be orthotropic. Without loss of generality, the diffusivity matrix can be described as,

$$\left\{D_{i,mn}^{S}\right\} = \begin{Bmatrix} D_{i,11}^{S} & D_{i,12}^{S} & D_{i,13}^{S} \\ D_{i,21}^{S} & D_{i,22}^{S} & D_{i,23}^{S} \\ D_{i,31}^{S} & D_{i,32}^{S} & D_{i,33}^{S} \end{Bmatrix} = \begin{Bmatrix} D_{i,11}^{S} & 0 & 0 \\ 0 & D_{i,11}^{S} & 0 \\ 0 & 0 & D_{i,33}^{S} \end{Bmatrix} = D_{i,33}^{S} \begin{Bmatrix} d_{i,\mathrm{aniso}} & 0 & 0 \\ 0 & d_{i,\mathrm{aniso}} & 0 \\ 0 & 0 & 1 \end{Bmatrix}, \quad (13)$$

where $d_{i,\mathrm{aniso}} = D_{i,11}^{S}/D_{i,33}^{S}$. Liquid phase has usually isotropic diffusivity, thus,

$$\left\{D_{i,mn}^{L}\right\} = \begin{Bmatrix} D_{i,11}^{L} & D_{i,12}^{L} & D_{i,13}^{L} \\ D_{i,21}^{L} & D_{i,22}^{L} & D_{i,23}^{L} \\ D_{i,31}^{L} & D_{i,32}^{L} & D_{i,33}^{L} \end{Bmatrix} = \begin{Bmatrix} D_{i,11}^{L} & 0 & 0 \\ 0 & D_{i,11}^{L} & 0 \\ 0 & 0 & D_{i,11}^{L} \end{Bmatrix} = D_{i,11}^{L} \begin{Bmatrix} 1 & 0 & 0 \\ 0 & 1 & 0 \\ 0 & 0 & 1 \end{Bmatrix}. \quad (14)$$

Since all species, either Na^+ or Cs^+, have larger diffusivities in the liquid phase than in the solid phase, we assumed they have the same diffusivity in the liquid phase, i.e., $D_{1,11}^{L} = D_{2,11}^{L} = D_0^{L}$. But they may have very different diffusivities in the solid phase. Thus, we used

$$d_{\mathrm{ratio}} = D_{2,33}^{S}/D_{1,33}^{S} \quad (15)$$

to denote the diffusivity difference of the two species.

For the case that the dielectric permittivity is isotropic, the dielectric permittivity tensor can be described as $\varepsilon_{mn}^{S} = \varepsilon_0^{S}\delta_{mn}$ and $\varepsilon_{mn}^{L} = \varepsilon_0^{L}\delta_{mn}$ where δ_{mn} is the Kronecker delta function, $\delta_{mn} = 1$ when $m = n$ and $\delta_{mn} = 0$ when $m \neq n$.

Solving eqs. (1) and (8) under given boundary conditions and initial conditions, we have the evolution of electric field $\varphi(\mathbf{r}, t)$ and concentration fields $c_i(\mathbf{r}, t)$, hence, the uptake amount and ion exchange kinetics.

3. Numerical methods

In the simulations, the following normalizations were used: $\mathbf{r}^* = \frac{\mathbf{r}}{l_0}$, $t^* = \frac{tD_0}{l_0^2}$, where l_0, $D_0 = D_{1,33}^{S}$ are the characteristic length and diffusivity, respectively. By letting $\varphi^* = \frac{\epsilon_0\varphi}{l_0^2\Omega}$, the electrostatic potential equation (8) is replaced with

$$\nabla^* \cdot [\boldsymbol{\varepsilon}(\mathbf{r})\nabla^*\varphi^*] + \rho^*(\mathbf{r}) = 0, \tag{8'}$$

where $\nabla^* = l_0\nabla$, and

$$\rho^*(\mathbf{r}) = \sum_{i=1}^{2} z_i[c_i(\mathbf{r}) - c_i^0(\mathbf{r})]. \tag{6'}$$

Then, equation (7) is rewritten as

$$\mu_i^* = \mu_i/RT = \left[\sum_{\alpha=1}^{N} A_i(\alpha)\left(c_i - c_i^{eq}(\alpha)\right)\eta_\alpha + E_{\text{scale}}\, z_i\varphi^*\right], \;\; i = 1,2, \tag{7'}$$

where $E_{\text{scale}} = \frac{l_0^2\Omega F_c}{RT\epsilon_0}$ is a dimensionless quantity. The normalized evolution equation (1) becomes

$$\frac{\partial c_i(\mathbf{r}^*,t^*)}{\partial t^*} = \nabla^* \cdot \left(D_i^*\nabla^*(\mu_i^*)\right), \quad i = 1, \mathrm{Na}^+; i = 2, \mathrm{Cs}^+. \tag{1'}$$

The equation number with prime refers to the equation with the same number but being normalized.

A representative volume element (RVE) with a dimension of $128l_0 \times 128\ l_0 \times 128\ l_0$ was used. That means, the RVE was divided into 128×128×128 uniform grids and l_0 is the length between the nearest two grids. Periodic boundary conditions were applied in all directions. An iteration method [32] was used to numerically solve eq. (8'). The fast Fourier spectral method [33] for spatial discretization and a forward Euler scheme for time derivatives were employed to solve eq. (1').

4. Model parameters in idealized batch experiment

Since ion diffusion in the solution is much faster than that in the particle phases (zeolite) we assumed that Cs^+ and Na^+ are always uniformly distributed in solution. In the simulations, to increase the simulation efficiency we used a small RVE by reducing the volume of the liquid solution phase. Thus, the liquid phase volume fraction in the RVE is much less than that in a real batch test. To ensure that the simulation is equivalent to the batch test, we scaled the uniform concentration in the liquid solution by the solution volume in the batch test. The uniform concentration in the solution can be calculated as:

$$c_1^{\mathrm{BC}}(t)\big|_{\Phi=0} = \frac{\mathbb{C}_{1,total}(t)}{V_L}, \;\; c_2^{\mathrm{BC}}(t)\big|_{\Phi=0} = c_2^0(L) - \frac{\mathbb{C}_{2,total}(t)}{V_L}. \tag{16}$$

In eq. (16), V_L is the liquid solution volume in the batch test. $\Phi = 0$ represents the liquid solution phase. $\mathbb{C}_{1,total}$ is the total amount of Na^+ entering the liquid solution phase, and $\mathbb{C}_{2,total}$ is the total amount of Cs^+ entering the particle phase. They can be calculated by

$$\mathbb{C}_{1,total} = c_1^0(S)V_S - \int_{V_S} c_1(\mathbf{r},t)dV_S, \quad (17)$$

$$\mathbb{C}_{2,total} = \int_{V_S} c_2(\mathbf{r},t)dV_S, \quad (18)$$

where V_S is the total particle phase volume in the batch test. $c_1^0(S)$ is the initial concentration of c_1 (i.e., c_{Na^+}) inside of the particles and $c_2^0(L)$ is the initial concentration of c_2 (i.e., c_{Cs^+}) in the liquid solution. Equation (16) can be regarded as time-dependent Dirichlet boundary conditions for the solid phase domain which were used for all simulations.

Consider a batch test where 30-mg of Cs^+ adsorbent are added to a solution of 100-mL containing an initial Cs^+ concentration varying from 0.35 mmol/L to 14.0 mmol/L[34]. That means, in the batch test, the total Cs^+ content is about 0.035~1.4 mmol. Assume the Cs^+ adsorbent particles have a density of 461kg/m^3 with the concentration of Na^+ of 0.365 mmol/cm^3=0.365 mol/L. Therefore, 30-mg Cs adsorbent has a volume of 0.065cm^3 and a content of 0.024 mmol Na^+. The Na^+ concentration in the adsorbent particles corresponds to the amount of Cs^+ that can be completely exchanged from the solution with a ratio of 1:1 to account for the charge. Thus, its maximum exchange capacity is 0.8 mmol/g for Cs^+. In the following simulations, σ_0=0.365 mol/L is used to obtain normalized concentrations. These data are listed in Table 1.

Table 1. Material properties and initial concentrations.

Adsorbent particles		Cs^+ solution	
Na^+ concentration	$\sigma_0 = 0.365$ mol/L	Cs^+ concentration	(0.35~14.0)$\times 10^{-3}$ mol/L
Normalized concentration	$c_1^0(S) = 1.0$	Normalized concentration	$c_2^0(L)$ =0.00096~0.0384
Volume V_S	0.065 mL	Volume V_L	100 mL
Mass of adsorbent	30 mg	Mass of Cs^+	(0.035~1.4) mmol
Exchange capacity	0.8mmol (Na^+) / g (adsorbent)		106 mg Cs^+/ g (adsorbent)

Table 2. Model parameters.

Concentration	$c_1 = c_{Na^+}, z_1 = 1$	Liquid	Solid

	$c_2 = c_{\mathrm{Cs}^+}, z_2 = 1$	($\alpha = 1$ or L)	($\alpha = 2, \cdots, N$ or S)
Initial	$c_1^0(\alpha)$	0.0001	1.0
Initial	$c_2^0(\alpha)$	(0.00096~0.0384)	0.00001
Equilibrium (after ion exchange)	$c_1^{eq}(\alpha)$	0.001	0.001 (assumed solubility)
Equilibrium	$c_2^{eq}(\alpha)$	0.0002	1.0
potential coefficient	$A_1(\alpha), \mathrm{Na}^+$	2×10^3	2×10^3
	$A_2(\alpha), \mathrm{Cs}^+$	$(1\sim6) \times 10^3$	2×10^3
Dielectric permittivity	ε_0^α	175.0	175.0
Inhomogeneous coefficient	$d_{i,\mathrm{inh}}$	0.0	(0~-0.999)
Ratio of diffusivities	$d_{\mathrm{ratio}} = D_{2,33}^S / D_{1,33}^S$	N/A	(1.0~0.1)
Anisotropic coefficient	$d_{i,\mathrm{aniso}} = \frac{D_{i,11}^S}{D_{i,33}^S} = \frac{D_{i,22}^S}{D_{i,33}^S}$	N/A	(1.0~0.01)
Electric interaction coefficient	$E_{\mathrm{scale}} = l_0^2 \Omega F_c / (RT\epsilon_0)$	$(0\sim4 \times 10^7)$	$(0\sim4 \times 10^7)$
Coefficients	k	20.0	20.0
in eq. (5)	a_k	0.4	0.4

5. Results of ion exchange

We started the simulation by considering a spherical particle with a volume fraction 1.07% of the simulation cell $(128\ l_0)^3$. Its radius is about $17.5 l_0$. Assume the considered spherical particle has a radius of 200 μm. Then l_0= 11.4 μm. Table 2 lists the dimensionless parameters used in the simulations with a time step of $\Delta t^* = 1.0 \times 10^{-6}$.

The model parameters were given in Table 2 except $A_2(L)$, $c_2^0(L)$, $d_{i,\mathrm{inh}}$, d_{ratio}, $d_{i,\mathrm{aniso}}$, and E_{scale}. The notations of $\alpha = 1$ or L indicating liquid phase and $\alpha = 2, \cdots, N$ or S indicating solid phase is used consistently throughout the manuscript as well as Table 2. These parameters represent the chemical potential coefficient $A_2(L)$ of Cs^+ in the liquid phase, the initial Cs^+ concentration $c_2^0(L)$ in the liquid phase, the diffusion inhomogeneous coefficient $d_{i,\mathrm{inh}}$ in eq. (5),

the ratio of diffusivities of the two exchange ions in the solid phase d_{ratio}, the anisotropic coefficient $d_{i,\text{aniso}}$, and the effective coefficient of electric potential E_{scale} , respectively. In the following we demonstrated their effects on the kinetics of ion exchange. The ion exchange was quantified by the normalized quantity of Na^+ that has left the solid phase

$$Q_1(t) = \mathbb{C}_{1,total}(t)/(c_1^0(S)V_S), \tag{19}$$

and the normalized quantity of Cs^+ that has entered the solid phase

$$Q_2(t) = \mathbb{C}_{2,total}(t)/(c_1^0(S)V_S). \tag{20}$$

$Q_1(t)$ and $Q_2(t)$ quantities were normalized by the initial total Na^+ in the solid phase.

5.1 Effect of the Cs^+ chemical potential and initial concentration in the solution phase

For a given equilibrium concentration of Cs^+ in the solution phase, the free energy coefficient $A_2(L)$ and initial concentration $c_2^0(L)$ of Cs^+ determines the chemical potential of Cs^+ as described by eq. (7), hence, the diffusion driving force. In the simulations, a spherical particle with a radius of $17.5l_0$, which sits at the center of the simulation cell $128l_0 \times 128l_0 \times 128l_0$, was considered. We fixed the model parameters ($d_{\text{ratio}} = 1.0$, $d_{i,\text{aniso}} = 1.0$, $d_{i,\text{inh}} = 0.0$, and $E_{\text{scale}} = 0.0$), and studied the effect of $A_2(L)$ and $c_2^0(L)$ on ion exchange kinetics by ignoring the effect of charge ($E_{\text{scale}} = 0.0$). The quantities Q_1 (Na^+ released into the liquid) and Q_2 (Cs^+ absorbed into the solid) versus time are shown in Fig. 4. In all cases evaluated, the Na^+ released into the liquid approaches 100% of the initial concentration in the particle. It is found from Fig. 4(a) that the uptake kinetics of Cs^+, i.e., Q_2, decreases with the increase of $A_2(L)$ while the release kinetics of Na^+ is independent of $A_2(L)$. From eq. (7), increasing $A_2(L)$ increases the diffusion driving force which should speed up the diffusion of Cs^+ in the solution phase. However, across the interface, Cs^+ diffuses from a lower concentration region (liquid) to a higher concentration region (solid). Increasing $A_2(L)$ in eq. (7) increases the chemical potential barrier which slows down the diffusion of Cs^+ across the interface. Therefore, the overall uptake kinetics of Cs^+ is controlled by the competition between diffusion driving force and chemical potential barrier at the interface. For the given model parameters, increasing $A_2(L)$ slow down the ion exchange kinetics. Increasing the initial Cs^+ concentration increases the diffusion driving force in the liquid phase but does not affect the free energy, hence, the chemical potential barrier at the interface. As expected, increasing the initial Cs^+ concentration speeds up the uptake kinetics of

Cs^+ as shown in Fig. 4(b). The same effect of the initial Cs^+ concentration on the uptake kinetics of Cs^+ was observed in hexacyanoferrate loaded onto silica[35].

In Fig. 4, we can see that in most cases the total amount Q_2 of Cs^+ uptake is not equal to the total amount Q_1 of Na^+ release. When a sodium ion (Na^+) releases from the particle a negative charge vacancy is left behind. $Q_1 > Q_2$ means that the particle has a negative charge. The results reveal that if the effect of charge is not considered, the charge neutrality inside the particle is not maintained and would generate an electric field.

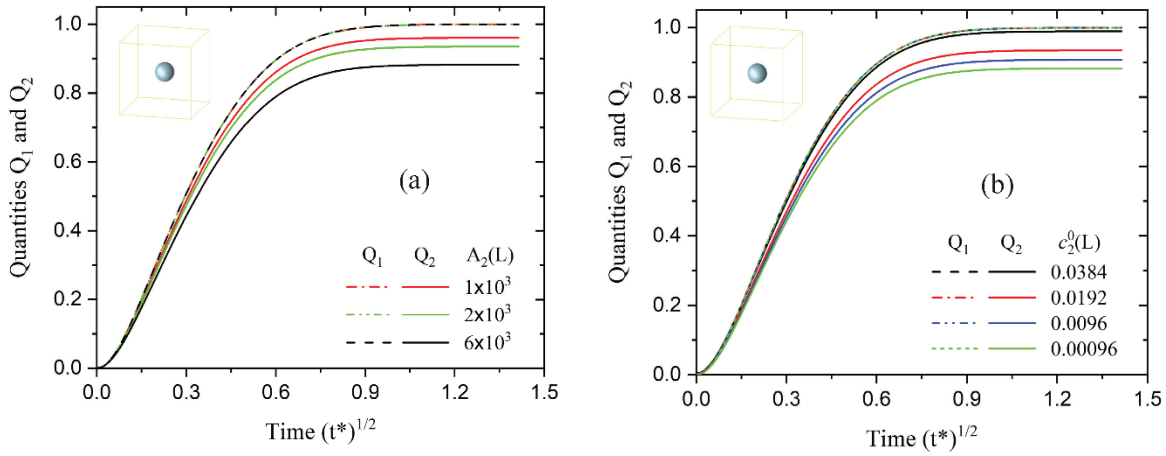

Fig. 4. Ion exchange of Na^+ (Q_1) and Cs^+ (Q_2) versus square root normalized time (a) as a function of $A_2(L)$; (b) as a function of $c_2^0(L)$. The inset image was the simulation cell with a spherical particle.

5.2 Effect of ion charge

By setting E_{scale} to a non-zero value, we turn on the effect of the electric field associated with the charge accumulation on ion exchange in the model. In addition, inhomogeneous diffusion of Cs^+ ions was considered for two cases with $d_{i,\text{inh}} = 0.0$ and -0.999, respectively. From eqs. (3-5), $d_{i,\text{inh}} = 0.0$ means that ion diffusivity only depends on the phase (solid, interface, or liquid); $d_{i,\text{inh}} = -0.999$ means that the diffusivity of ion i depends on both the phase and Cs^+ concentration. When Cs^+ concentration reaches the equilibrium concentration in the zeolite solid phase, both diffusivities of Na^+ and Cs^+ decrease by about three orders of magnitude. The concentration dependent diffusivity aims to describe the physics that an ion

(Cs^+) with a larger size replacing a smaller ion (Na^+) causes lattice distortions and creates a compressive stress that increases the diffusion barrier.

With the same simulation cell in section 5.1, $c_2^0(L) = 0.00096$, $A_2(L) = 6 \times 10^3$, $d_{\text{ratio}} = 1.0$ and $d_{i,\text{aniso}} = 1.0$ were used to assess the impact of charge density. The results were plotted in Fig. 5. It is observed that for both cases Na^+ release (Q_1) and Cs^+ uptake (Q_2) approach the same kinetics (overlaid lines in blue) when the contribution of static electric energy to the electrochemical potential increases, i.e., as E_{scale} increases. $Q_1(t) = Q_2(t)$ means that the overall charge inside the particle remains at zero during ion exchange. For the cases with E_{scale} =0.0, 4×10^7 and $d_{i,\text{inh}} = 0.0, -0.999$, the ion charge density distributions at the late stage (i.e., $(t^*)^{1/2} = 1.41$) were plotted along a diameter direction of the spherical particle in Fig. 6. The ion charge density was regarded as zero in the liquid solution phase. When E_{scale} =4×10^7, the nearly zero charge density indicates charge neutrality inside the particle. When E_{scale} =0.0, the ion charge concentration can be seen in Fig. 6. When $d_{i,\text{inh}} = -0.999$, i.e., considering inhomogeneous diffusivity, the ion charge and therefore the ion concentration exhibit oscillations inside the particle. It is interesting to find that 1) the electric field slows down the faster process (Na^+ release) and speeds up the slower process (Cs^+ uptake); and 2) the ion kinetics dramatically slows down to maintain charge neutrality at the later stage. In experiments, it is observed that the full Na^+ capacity of the liquid was not reached, even after a long incubation times. Both concentration dependent diffusivity and charge neutrality slow down the ion exchange kinetics, which may explain the observed phenomena.

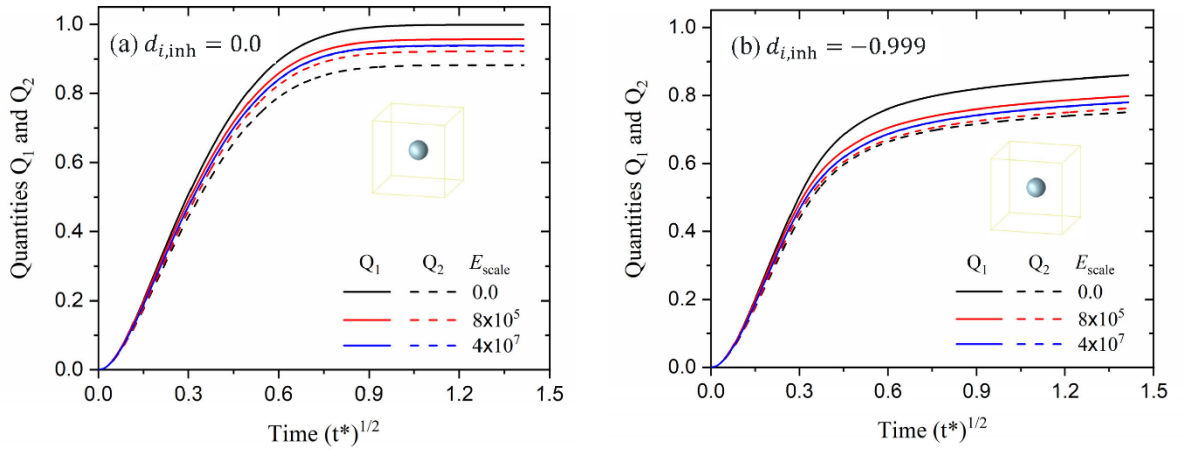

Fig. 5. Effect of electric potential field (E_{scale}) and concentration dependent diffusivity on ion exchange kinetics, (a) $d_{i,\text{inh}} = 0.0$; (b) $d_{i,\text{inh}} = -0.999$. The inset image was the simulation cell with a spherical particle.

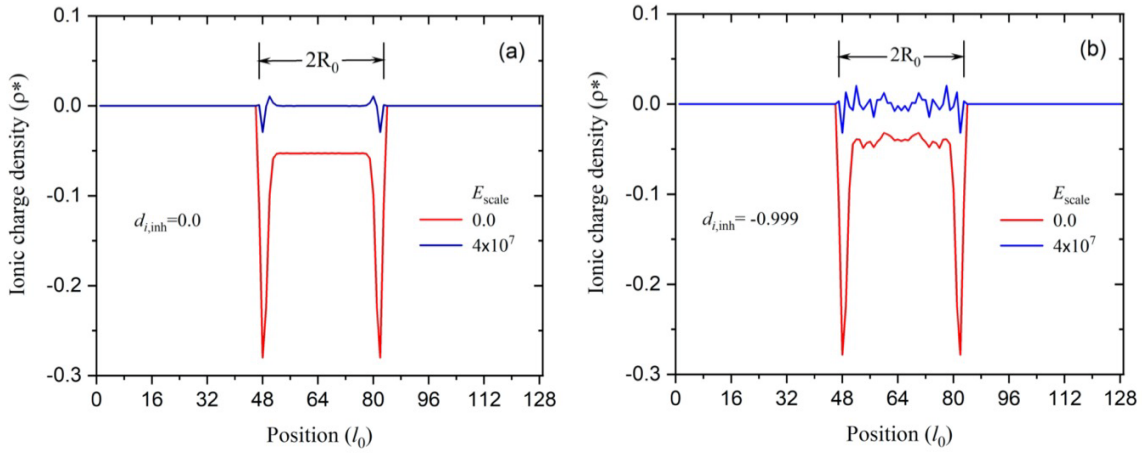

Fig. 6. Ion charge density (ρ^*) distribution along a diameter direction of the spherical particle at a late stage when $(t^*)^{1/2} = 1.41$, (a) $d_{i,\text{inh}} = 0.0$; (b) $d_{i,\text{inh}} = -0.999$.

5.3 Effect of diffusivity ratio d_{ratio}

The diffusivities of Cs^+ and Na^+ can be quite different because the ions have different atomic sizes. Figure 7 presents the effect of the diffusivity ratio d_{ratio} on the ion exchange kinetics in a spherical particle. In the simulations, $c_2^0(L) = 0.00096$, $A_2(L) = 6 \times 10^3$, $d_{i,\text{inh}} = -0.999$, and $E_{\text{scale}} = 4 \times 10^7$ were used. Na^+ diffusivity was assumed to remain the same while different $d_{\text{ratio}} = D_{2,33}^S / D_{1,33}^S = D_{Cs^+,33}^S / D_{Na^+,33}^S$ were used to describe the Cs^+ diffusivity. Generally, the Cs^+ species has a smaller diffusivity than Na^+. It is found that 1) $Q_1(t)$ and $Q_2(t)$ are almost the same for the entire process, i.e., the particle maintains charge neutrality; and 2) decreasing Cs^+ diffusivity significantly slows down the ion exchange kinetics. The uptake kinetics of Cs^+ is controlled by Cs^+ diffusivity, the slower diffusive species.

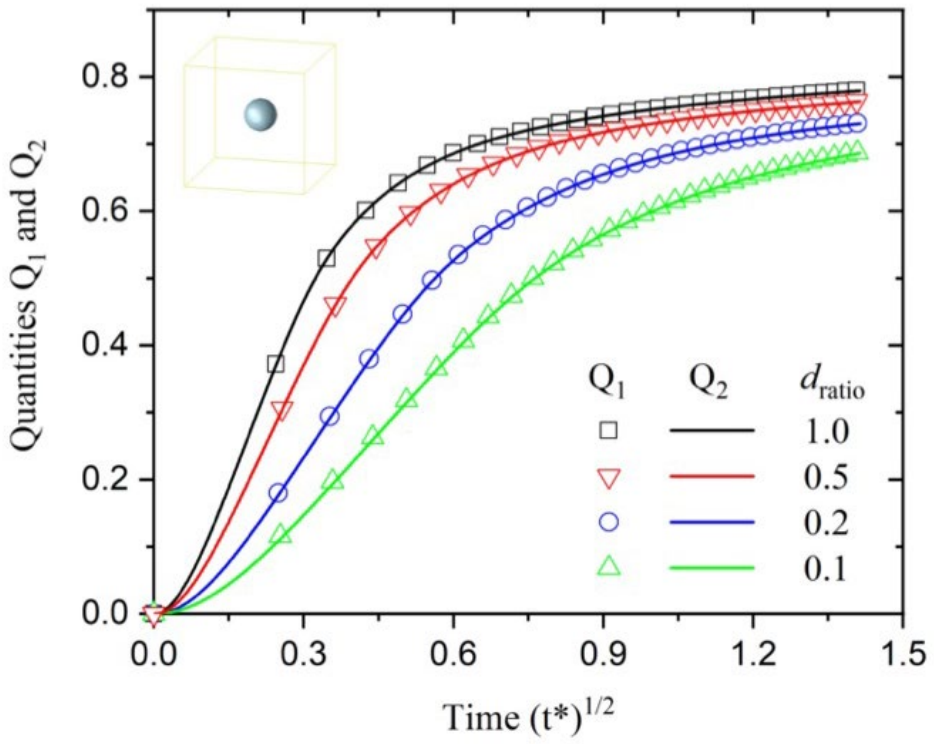

Fig. 7. Quantities Q_1 and Q_2 versus time and the diffusivity ratio of $d_{\text{ratio}} = D^S_{\text{Cs}^+,33}/D^S_{\text{Na}^+,33}$. The inset image was the simulation cell with a spherical particle.

5.4 Effect of diffusivity anisotropy $d_{i,\text{aniso}}$

In crystals with tunnel structures, ions may have strongly anisotropic diffusivities. In this section, we studied the effect of diffusivity anisotropy $d_{i,\text{aniso}}$ on ion exchange kinetics in a tetragonal particle with dimension of $19l_0 \times 19l_0 \times 57l_0$ (i.e., a × b × c with a = b and c > a and b) at the center of the simulation cell. In these simulations, the direction of the fastest diffusion is along y_3(or c)-direction which is assigned to be $D^S_{i,33} = 1$. The diffusivity anisotropy is defined as $d_{i,\text{aniso}} = D^S_{i,11}/D^S_{i,33} = D^S_{\text{i},22}/D^S_{i,33}$. In the simulations, $c_2^0(L) = 0.00096$, $A_2(L) = 6 \times 10^3$, $d_{i,\text{inh}} = -0.999$, $d_{\text{ratio}} = 1.0$ and $E_{\text{scale}} = 4 \times 10^7$ were used. Figure 8(a) displays the uptake of Cs^+ versus time and diffusivity anisotropy. Since $E_{\text{scale}} = 4 \times 10^7$ ensures $Q_1(t) = Q_2(t)$, i.e., charge neutrality is always maintained; only $Q_2(t)$, the absorption of Cs^+, is shown in Fig. 8(a). The results in Fig. 8(a) demonstrate that the ion exchange kinetics is slowed with the decrease of $d_{i,\text{aniso}}$, i.e., as the diffusivity $D^S_{\text{i},11} = D^S_{\text{i},22}$ on the y_1-y_2 plane is reduced relative to the major axis (y_3 or c). For $d_{i,\text{aniso}} = 0.1$, the evolution

of Cs^+ distribution on the center y_2-y_3 plane is shown in Fig. 8(b). The diffusion distance along y_3 (or c)-direction is much longer than that along y_1 (or a)- and y_2 (or b)-directions. For a needle shaped particle, the faster diffusion direction or tunnel direction usually aligns with the needle (long) direction. The results indicate that the diffusivity in the plane normal to the needle direction significantly affects the ion exchange kinetics.

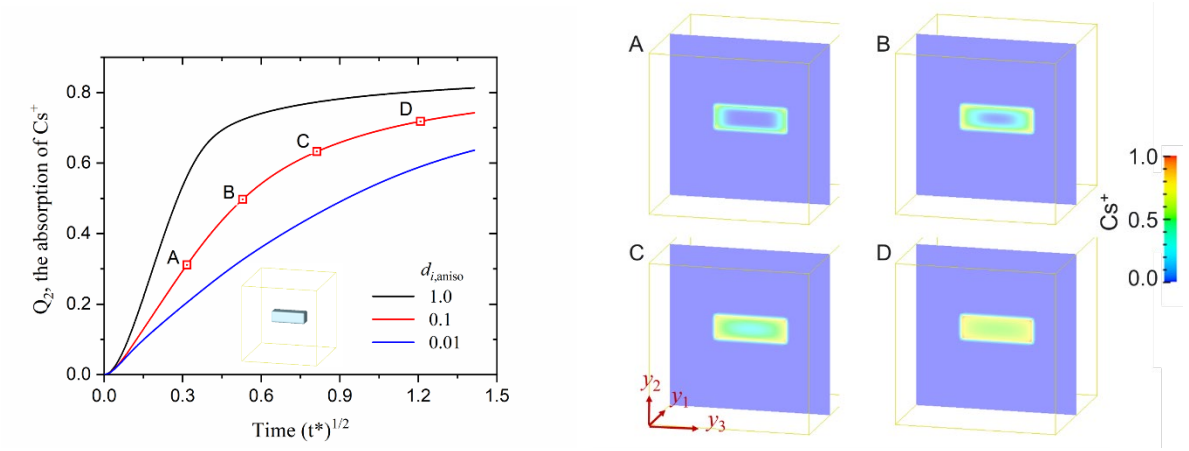

(a) (b)

Fig. 8. (a) uptake of Cs^+ versus diffusivity anisotropy $d_{i,\text{aniso}}$ for a tetragonal particle as shown in the inset image. (b) Cs^+ distributions on the center y_2-y_3 plane of the particle at the times marked by A, B, C, and D on the curve in Fig. 8(a) with $d_{i,\text{aniso}} = 0.1$.

5.5 Effect of particle shape

Particles with a same volume but different shapes have different surface areas, i.e., varying surface to volume ratios. Figure 9 displays the effect of particle surface area on the uptake kinetics of Cs^+. In these simulations, $c_2^0(L) = 0.00096$, $A_2(L) = 6 \times 10^3$, $d_{i,\text{inh}} = -0.999$, $d_{\text{ratio}} = 1.0$, and $E_{\text{scale}} = 4 \times 10^7$ were used. Five particles with different shapes (sphere, and tetragonal with aspect ratio a/c=2.0, 1.0. 0.33 and 0.23) were considered. Two cases of (a) isotropic diffusivity $d_{i,\text{aniso}} = 1.0$ and (b) anisotropic diffusivity $d_{i,\text{aniso}} = 0.1$ ($D_{i,33}^S > D_{i,11}^S$ and $D_{i,22}^S$) were simulated. For isotropic diffusivity properties, Fig. 9(a), shows that the uptake kinetics are controlled by the particle surface area. Particles with larger surface area relative to the volume (higher surface/volume ratio) have faster absorption rates. The spherical particle, which has smallest surface area for a given volume, has the slowest uptake kinetics. In

the anisotropic diffusivity case, Fig 9(b), however, both the surface area and the diffusion distance in the direction with the fastest diffusivity (the c-axis) are important. Increasing the surface area and decreasing the diffusion distance in the direction with the fastest diffusivity speed up the uptake kinetics. For the particles with a/c=1 and 2.0, the surface area increases and the diffusion distance in the direction with the fastest diffusivity decreases. It is found the uptake kinetics increases for this combination of particle shape and diffusion anisotropy. For the particles with spherical, tetragonal of a/c=0.33 to a/c=0.23 shapes, both the surface area and the diffusion distance in the direction with the fastest diffusivity increase, however, the uptake kinetics decreases. Therefore, a needle-shaped particle with the tunnel along the needle direction may have slow uptake kinetics if the diffusivity on the plane normal to the needle direction is extremely small. A needle-like particle with faceted surfaces, which usually have a high atom density, may have extremely small diffusivity in the normal direction of the faceted surface.

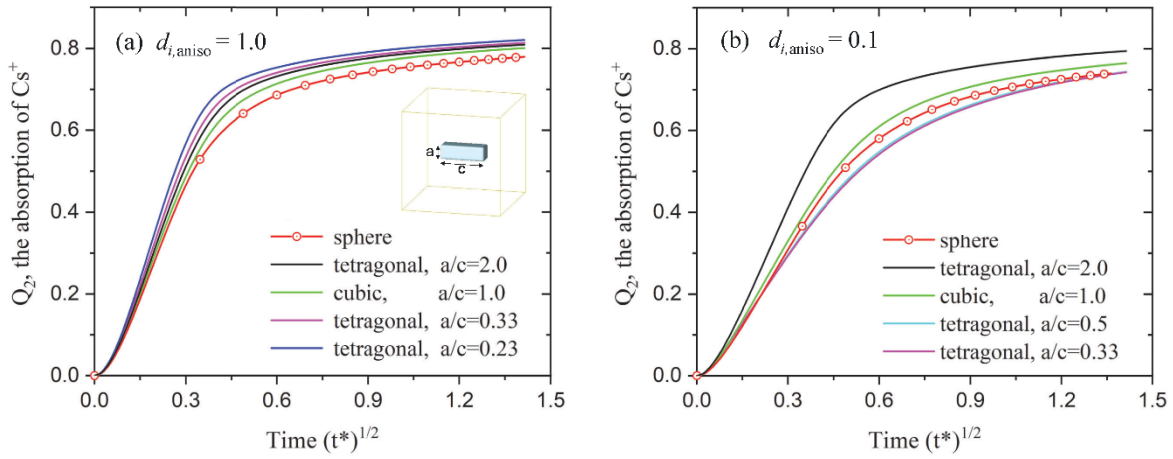

Fig. 9. Effect of particle shape on the absorption of Cs^+ (a) $d_{i,\text{aniso}} = 1.0$ and (b) $d_{i,\text{aniso}} = 0.1$. The inset image was the simulation cell with a tetragonal particle.

5.6 Effect of particle aggregation

Fig. 10(a) displays a particle aggregation/cluster used for simulating the effect of particle aggregation; A phase-field model of precipitation has been used to generate clusters of needle-like particles. In the particle aggregation/cluster simulation, the ratio of liquid volume (V_L) and solid volume (V_S) is the same for the particle cluster as for a single particle. The single particle case can be regarded as a particle cluster with particles well separated from each other. With the

developed model, the effect of particle aggregation on uptake kinetics of Cs^+ was simulated with the model parameters $c_2^0(L) = 0.00096$, $A_2(L) = 6 \times 10^3$, $d_{i,\text{inh}} = -0.999$, $d_{\text{ratio}} = 1.0$, and $E_{\text{scale}} = 4 \times 10^7$. The particles have a tetragonal shape with a/c=1/3 and a=5.5l_0. Fig. 10(b) shows the comparison of the Cs^+ uptake kinetics in the single particle and particle cluster cases. The dashed lines represent the uptake kinetics in the single particle or particles well separated while the solid lines for the particle cluster. Two observations can be seen with these results. First, the uptake kinetics in the cluster is slower than that in the single particle. The results show that increasing surface area (particles well separated) increases the uptake kinetics. Second, decreasing the diffusivity along the short edges, i.e., the y_1 and y_2 directions of the faceted particle decreases the uptake kinetics. We also evaluated the Cs^+ distribution and the charge neutrality in the cluster during the ion exchange process. Figure 11 displays the spatial distribution of Cs^+ and its evolution with time at a cross-section of the simulation cell. Heterogeneous distribution of Cs^+ within the cluster illustrates the particle aggregation effect.

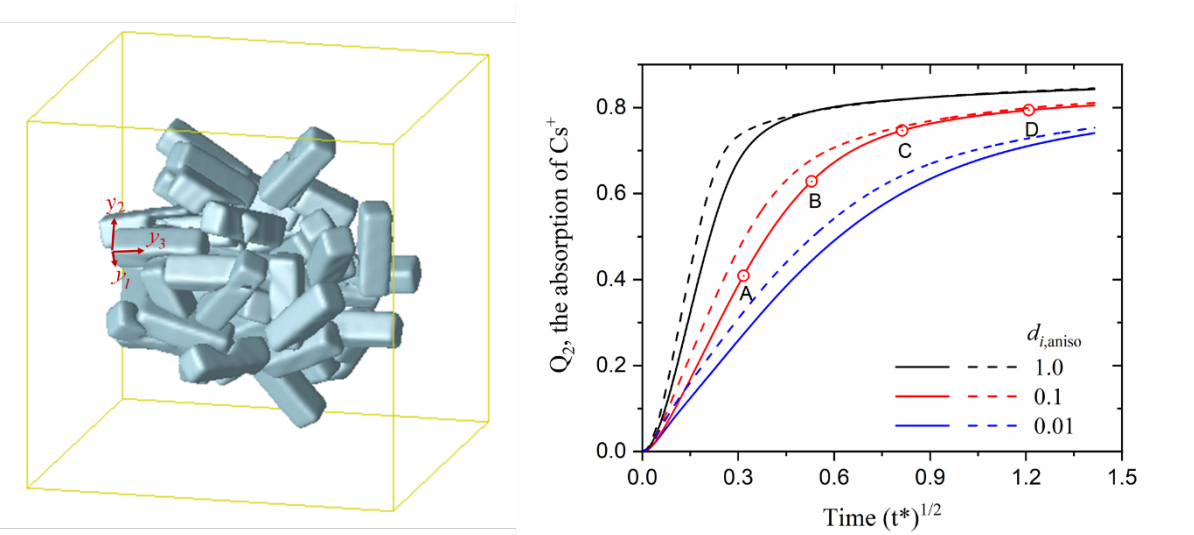

(a) (b)

Fig. 10. (a) Particle aggregation/cluster; (b) Absorption of Cs^+ as a function of diffusivity anisotropy. The tetragonal particles are of a/c=1/3 and a=5.5l_0. $d_{i,\text{aniso}} = D^S_{i,\text{short edge}}/D^S_{i,\text{long edge}} = D^S_{i,y_1}/D^S_{i,y_3}$.The dashed lines are the corresponding results for the same size of tetragonal particles but each particle well-separated from the others.

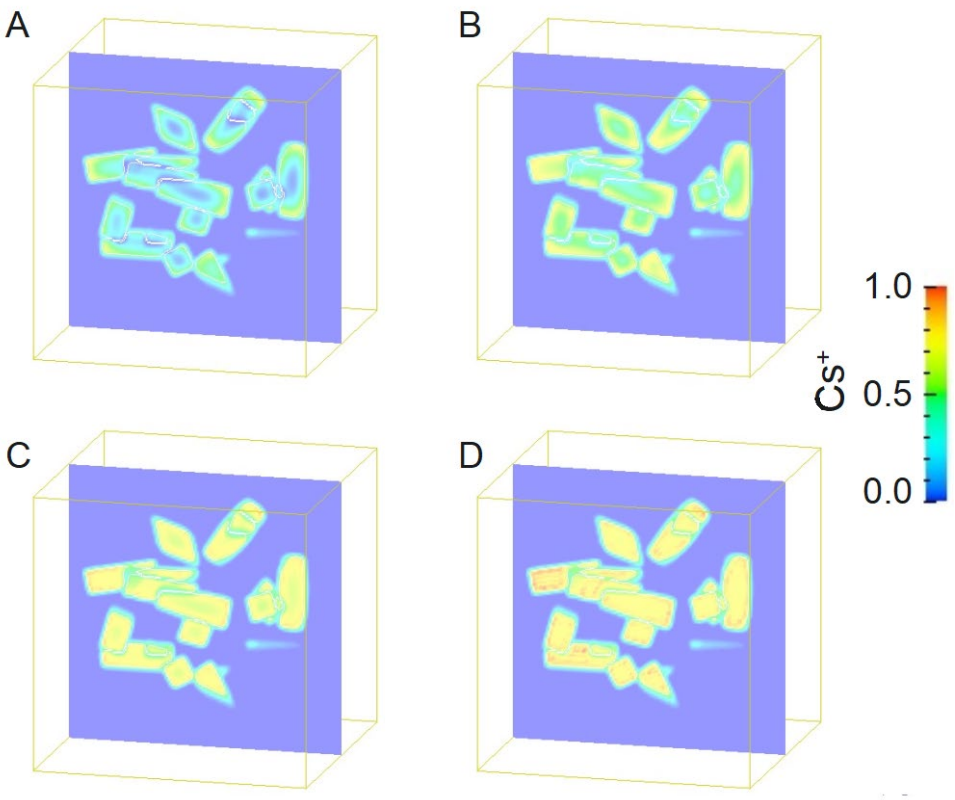

Fig. 11. The distributions of Cs^+ for the case $d_{i,\mathrm{aniso}} = 0.1$ at the stages A, B, C, and D which were denoted in Fig. 10(b).

6. Conclusions

In this work, we developed a mesoscale model of ion exchange in a particle cluster for batch experimental conditions. The model considered the inhomogeneous and anisotropic diffusivity in the particles and the electric field associated with ion accumulation. The effect of thermodynamic and kinetic properties, particle morphology and particle aggregation on the uptake kinetics, the evolution of ion charge, and electric field were systematically simulated. It is found that 1) ion exchange produces charge accumulation inside the particle because different ions have different diffusivities and different diffusion driving forces. The electric neutrality is not maintained; 2) the electric field speeds up the slower kinetics (ion uptake or ion release) and slows down the faster kinetics to reduce the charge accumulation and preserves charge neutrality; 3) the ion exchange becomes very slow in the later stages because a) the diffusion driving force (electrochemical gradient, Cs^+ concentration in the solution and Na^+ inside the particle) continuously decreases, as found in the batch experiments, and b) the diffusivity

decreases due to the Cs^+ concentration dependence on ion diffusivity. This can explain the experimental observation that usually the maximum radionuclide adsorption capacity cannot be reached; 4) for needle-like particles and their clusters, both surface area and diffusion distance in the direction with the fastest diffusivity significantly impact the ion exchange kinetics. These results demonstrate that the developed model can be used to perform a systematic parametric study about the effect of particle morphology, particle aggregation, particle anisotropic and inhomogeneous kinetics properties on ion exchange kinetics.

Accurate thermodynamic properties including the free energies of different phases, concentration dependent diffusivities of species, and electronic properties are required to quantitatively validate the modeling approach described herein. In our Energy Frontier Research Center (the Center for Hierarchical Waste Form Materials, an EFRC funded by the U.S. Department of Energy) (https://science.osti.gov/bes/efrc/Centers/chwm) measurements and evaluations of zeolite thermodynamic and kinetic properties are under way. Calorimetry is used to measure the formation enthalpies of zeolites with different Si/Al ratios and to study phase stability. The extra-framework cation locations in zeolites is investigated by X-ray diffraction (XRD) to correlate Na^+, H^+ and Cs^+ accessibilities and thermodynamic stabilities. Density functional theory calculations are used to probe the incorporation of Cs^+, H^+ and Na^+ ions into zeolites to determine energies for exchange and lattice stabilities [36, 37]. And kinetics and adsorption isotherms and specific Cs^+ selectivity are measured by batch experiments [38]. All these data are important for quantitatively modeling and providing guidance on the design of hierarchical wasteforms with the desire to improve ion exchange efficiencies and increase radionuclide capacities.

Acknowledgements

The work described in this article was performed by Pacific Northwest National Laboratory, which is operated by Battelle for the U.S. Department of Energy under Contract DE-AC05-76RL01830. This work was supported as part of the Center for Hierarchical Waste Form Materials, an Energy Frontier Research Center funded by the U.S. Department of Energy, Office of Science, Basic Energy Sciences under Award No. DE-SC0016574. Computations were performed on Constance cluster at Pacific Northwest National Laboratory.

References

[1] R.J. Budnitz, Strontium-90 and strontium-89: a review of measurement techniques in environmental media, 1974, http://inis.iaea.org/search/search.aspx?orig_q=RN:06179644.

[2] M.I. Ojovan, W.E. Lee, An Introduction to Nuclear Waste Immobilisation, Elsevier, Oxford, UK, 2014.

[3] H.-C. zur Loye, T. Besmann, J. Amoroso, K. Brinkman, A. Grandjean, C.H. Henager, S. Hu, S.T. Misture, S.R. Phillpot, N.B. Shustova, H. Wang, R.J. Koch, G. Morrison, E. Dolgopolova, Hierarchical Materials as Tailored Nuclear Waste Forms: A Perspective, Chemistry of Materials 30(14) (2018) 4475-4488.

[4] T. Frising, P. Leflaive, Extraframework cation distributions in X and Y faujasite zeolites: A review, Micropor Mesopor Mat 114(1-3) (2008) 27-63.

[5] B. Said, A. Grandjean, Y. Barre, F. Tancret, F. Fajula, A. Galarneau, LTA zeolite monoliths with hierarchical trimodal porosity as highly efficient microreactors for strontium capture in continuous flow, Microporous and Mesoporous Materials 232 (2016) 39-52.

[6] K. Yoshida, K. Toyoura, K. Matsunaga, A. Nakahira, H. Kurata, Y.H. Ikuhara, Y. Sasaki, Atomic sites and stability of Cs+ captured within zeolitic nanocavities, Scientific Reports 3(1) (2013) 2457.

[7] M.Y. Prajitno, M. Taufiqurrakhman, D. Harbottle, T.N. Hunter, Kinetic Studies of Cs+ and Sr2+ Ion Exchange Using Clinoptilolite in Static Columns and an Agitated Tubular Reactor (ATR), ChemEngineering 5(1) (2021) 9.

[8] K.S. Hwang, C.W. Park, K.W. Lee, S.J. Park, H.M. Yang, Highly efficient removal of radioactive cesium by sodium-copper hexacyanoferrate-modified magnetic nanoparticles, Colloids and Surfaces a-Physicochemical and Engineering Aspects 516 (2017) 375-382.

[9] H.M. Yang, K.S. Hwang, C.W. Park, K.W. Lee, Sodium-copper hexacyanoferrate-functionalized magnetic nanoclusters for the highly efficient magnetic removal of radioactive caesium from seawater, Water Res 125 (2017) 81-90.

[10] S. Szöke, G. Pátzay, L. Weiser, Development of selective cobalt and cesium removal from the evaporator concentrates of the PWR Paks, Radiochimica Acta 91(4) (2003) 229-232.

[11] C. Loos-Neskovic, S. Ayrault, V. Badillo, B. Jimenez, E. Garnier, M. Fedoroff, D.J. Jones, B. Merinov, Structure of copper-potassium hexacyanoferrate (II) and sorption mechanisms of cesium, J Solid State Chem 177(6) (2004) 1817-1828.

[12] X. Wang, S. Pandey, M. Fullarton, S.R. Phillpot, Study of Incorporating Cesium into Copper Hexacyanoferrate by Density Functional Theory Calculations, The Journal of Physical Chemistry C 125(43) (2021) 24273-24283.
[13] I.W. Donald, B.L. Metcalfe, R.N.J. Taylor, The immobilization of high level radioactive wastes using ceramics and glasses, Journal of Materials Science 32(22) (1997) 5851-5887.
[14] P. Tumurugoti, S.K. Sundaram, S.T. Misture, Cesium immobilization in (Ba,Cr)-hollandites: Effects on structure, J Solid State Chem 258 (2018) 72-78.
[15] D. Caurant, P. Loiseau, O. Majerus, V. Aubin-Chevaldonnet, I. Bardez, A. Quintas, Glasses, glass-ceramics and ceramics for immobilization of highly radioactive nuclear wastes, Nova Science Hauppauge2007.
[16] A.E. Ringwood, S.E. Kesson, N.G. Ware, W. Hibberson, A. Major, Immobilisation of high level nuclear reactor wastes in SYNROC, Nature 278(5701) (1979) 219-223.
[17] F. Rabbi, K. Brinkman, J. Amoroso, K. Reifsnider, Finite element analysis of ion transport in solid state nuclear waste form materials, Journal of Nuclear Materials 493 (2017) 303-309.
[18] A.A. Berseneva, C.R. Martin, V.A. Galitskiy, O.A. Ejegbavwo, G.A. Leith, R.T. Ly, A.M. Rice, E.A. Dolgopolova, M.D. Smith, H.-C. zur Loye, D.P. DiPrete, J.W. Amoroso, N.B. Shustova, “Boarding-Up”: Radiation Damage and Radionuclide Leaching Kinetics in Linker-Capped Metal–Organic Frameworks, Inorganic Chemistry 59(1) (2020) 179-183.
[19] G. Morrison, M.D. Smith, H.C. zur Loye, Understanding the Formation of Salt-Inclusion Phases: An Enhanced Flux Growth Method for the Targeted Synthesis of Salt-Inclusion Cesium Halide Uranyl Silicates, J Am Chem Soc 138(22) (2016) 7121-7129.
[20] A. Merceille, E. Weinzaepfel, Y. Barré, A. Grandjean, Effect of the synthesis temperature of sodium nonatitanate on batch kinetics of strontium-ion adsorption from aqueous solution, Adsorption 17(6) (2011) 967-975.
[21] E. Jaramillo, C.P. Grey, S.M. Auerbach, Molecular dynamics studies of hydrofluorocarbons in faujasite-type zeolites: Modeling guest-induced cation migration in dry zeolites, Journal of Physical Chemistry B 105(49) (2001) 12319-12329.
[22] C. Abrioux, B. Coasne, G. Maurin, F. Henn, M. Jeffroy, A. Boutin, Cation Behavior in Faujasite Zeolites upon Water Adsorption: A Combination of Monte Carlo and Molecular Dynamics Simulations, The Journal of Physical Chemistry C 113(24) (2009) 10696-10705.

[23] D. Enke, R. Glaser, U. Tallarek, Sol-Gel and Porous Glass-Based Silica Monoliths with Hierarchical Pore Structure for Solid-Liquid Catalysis, Chemie Ingenieur Technik 88(11) (2016) 1561-1585.
[24] H.Y. Lee, H.S. Kim, H.-K. Jeong, M. Park, D.-Y. Chung, K.-Y. Lee, E.-H. Lee, W.T. Lim, Selective Removal of Radioactive Cesium from Nuclear Waste by Zeolites: On the Origin of Cesium Selectivity Revealed by Systematic Crystallographic Studies, The Journal of Physical Chemistry C 121(19) (2017) 10594-10608.
[25] C.A. Juillerat, V.V. Klepov, M.D. Smith, H.C. Zur Loye, Targeted crystal growth of uranium gallophosphates via the systematic exploration of the UF4-GaPO4-ACl (A = Cs, Rb) phase space, Crystengcomm 22(17) (2020) 3020-3032.
[26] C.A. Juillerat, V. Kocevski, T.M. Besmann, H.C. zur Loye, Discovery of Cs-2(UO2)Al2O5 by Molten Flux Methods: A Uranium Aluminate Containing Solely Aluminate Tetrahedra as the Secondary Building Unit, Inorganic Chemistry 58(7) (2019) 4099-4102.
[27] G. Morrison, H.-C. zur Loye, Flux Growth of [NaK6F][(UO2)3(Si2O7)2] and [KK6Cl][(UO2)3(Si2O7)2]: The Effect of Surface Area to Volume Ratios on Reaction Products, Cryst Growth Des 16(3) (2016) 1294-1299.
[28] Y.L. Li, B.D. Zeidman, S.Y. Hu, C.H. Henager, T.M. Besmann, A. Grandjean, A physics-based mesoscale phase-field model for predicting the uptake kinetics of radionuclides in hierarchical nuclear wasteform materials, Computational Materials Science 159 (2019) 103-109.
[29] M. Jiménez-Reyes, P.T. Almazán-Sánchez, M. Solache-Ríos, Radioactive waste treatments by using zeolites. A short review, Journal of Environmental Radioactivity 233 (2021) 106610.
[30] Y.L. Li, S.Y. Hu, R. Montgomery, F. Gao, X. Sun, Phase-field simulations of intragranular fission gas bubble evolution in UO2 under post-irradiation thermal annealing, Nucl. Instrum. Methods Phys. Res. Sect. B-Beam Interact. Mater. Atoms 303 (2013) 62-67.
[31] D. Fan, L.Q. Chen, Computer simulation of grain growth using a continuum field model, Acta Materialia 45(2) (1997) 611-622.
[32] S.Y. Hu, L.Q. Chen, A phase-field model for evolving microstructures with strong elastic inhomogeneity, Acta Materialia 49(11) (2001) 1879-1890.
[33] L.Q. Chen, J. Shen, Applications of semi-implicit Fourier-spectral method to phase field equations, Comput. Phys. Commun. 108(2-3) (1998) 147-158.

[34] A.M. El-Kamash, Evaluation of zeolite A for the sorptive removal of Cs+ and Sr2+ ions from aqueous solutions using batch and fixed bed column operations, Journal of Hazardous Materials 151(2) (2008) 432-445.
[35] A. Grandjean, Y. Barré, A. Hertz, V. Fremy, J. Mascarade, E. Louradour, T. Prevost, Comparing hexacyanoferrate loaded onto silica, silicotitanate and chabazite sorbents for Cs extraction with a continuous-flow fixed-bed setup: Methods and pitfalls, Process Safety and Environmental Protection 134 (2020) 371-380.
[36] V. Kocevski, B.D. Zeidman, C.H. HenagerJr., T.M. Besmann, Communication: First-principles evaluation of alkali ion adsorption and ion exchange in pure silica LTA zeolite, The Journal of Chemical Physics 149(13) (2018) 131102.
[37] V. Kocevski, S.Y. Hu, T.M. Besmann, Alkaline earth ion exchange study of pure silica LTA zeolites using periodic first-principles calculations, New Journal of Chemistry 43(43) (2019) 16835-16840.
[38] V. Proust, A. Gossard, J. Schaeperkoetter, T. David, S.M. Misture, A. Grandjean, H.C. zur Loye, Crystalline/amorphous alumino-silicate composite for Cs entrapment: links between composition, structure and ion exchange efficiency, in preparation.